1   **Title:** Barth syndrome cellular models have dysregulated respiratory chain complex I and

2   mitochondrial quality control due to abnormal cardiolipin

3

4   **Authors:** Arianna F. Anzmann[a] (ORCID:0000-0002-7368-6918)**,** Olivia L. Sniezek[a]

5   (ORCID:0000-0002-6435-2852), Alexandra Pado[a] (ORCID:0000-0003-2018-0662), Veronica

6   Busa[a] (ORCID:0000-0002-3981-9975), Frédéric Maxime Vaz[b] (ORCID:0000-0002-9048-1041),

7   Simion D. Kreimer[c] (ORCID:0000-0001-6627-3771), Robert Norman Cole[c] (ORCID:0000-0002-

8   3096-4754), Anne Le[d] (ORCID:0000-0002-2958-8149), Brian James Kirsch[d] (ORCID:0000-

9   0001-9984-4438), Steven M. Claypool[e] (ORCID:0000-0001-5316-1623), Hilary J.

10 Vernon[a*](ORCID:0000-0001-9940-9866)

11

12 [a] Department of Genetic Medicine, Johns Hopkins University School of Medicine, Baltimore,

13 Maryland, USA

14 [b] Department of Clinical Chemistry and Pediatrics, Academic Medical Center, Amsterdam, The

15 Netherlands

16 [c] Mass Spectrometry and Proteomics Facility, Department of Biological Chemistry, Johns

17 Hopkins University School of Medicine, Baltimore, Maryland, USA.

18 [d] Department of Pathology and Oncology, Johns Hopkins University School of Medicine,

19 Baltimore, Maryland, USA

20 [e] Department of Physiology, Johns Hopkins University School of Medicine, Baltimore, Maryland,

21 USA

22 **Corresponding author at:** Department of Genetic Medicine, Johns Hopkins University School

23 of Medicine, 733 N Broadway, MRB 512 Baltimore, Maryland, USA. Email: hvernon1@jhmi.edu

24 (H.J. Vernon)

25

Abstract

Barth syndrome (BTHS) is an X-linked genetic condition caused by defects in *TAZ*, which encodes a transacylase involved in the remodeling of the inner mitochondrial membrane phospholipid, cardiolipin (CL). As such, CL has been implicated in numerous mitochondrial functions, and the role of defective CL in the clinical pathology of BTHS is under intense investigation. We used untargeted proteomics, shotgun lipidomics, gene expression analysis, and targeted metabolomics to identify novel areas of mitochondrial dysfunction in a new model of TAZ deficiency in HEK293 cells. Functional annotation analysis of proteomics data revealed abnormal regulation of mitochondrial respiratory chain complex I (CI), driven by the reduced abundance of 6 CI associated proteins in TAZ-deficient HEK293 cells: MT-ND3, NDUFA5, NDUFAB1, NDUFB2, NDUFB4*,* and NDUFAF1. This resulted in reduced assembly and function of CI in TAZ-deficient HEK293 cells as well as BTHS patient derived lymphoblast cells. We also identified increased abundance of PARL, a rhomboid protein involved in the regulation of mitophagy and apoptosis, and abnormal downstream processing of PGAM5, another mediator of mitochondrial quality control, in TAZ-deficient cells. Lastly, we modulated CL via the phospholipase inhibitor bromoenol lactone and the CL targeted SS-peptide, SS-31, and showed that each is able to remediate abnormalities in CI abundance as well as PGAM5 processing. Thus, mitochondrial respiratory chain CI and PARL/PGAM5 regulated mitochondrial quality control, both of whose functions localize to the inner mitochondrial membrane, are dysregulated due to TAZ deficiency and are partially remediated via modulation of CL.

Introduction

Barth syndrome (BTHS, MIM#302060) is a rare X-linked inborn error of mitochondrial phospholipid metabolism caused by variants in the gene TAFAZZIN (*TAZ*) (1–3). *TAZ* encodes a transacylase essential for the remodeling and maturation of the mitochondrial phospholipid cardiolipin (CL) (1, 4). CL, primarily localized to inner mitochondrial membrane, has many key functions, including roles in maintaining mitochondrial cristae structure, organization of respiratory complexes, protein import, fusion, fission, and cellular signaling (1). TAZ deficiency results in abnormal CL content, including an accumulation of the remodeling intermediate monolysocardiolipin (MLCL), decreased remodeled CL, and a shift towards saturated CL species (1, 5). An elevated MLCL:CL ratio is the pathognomonic metabolic defect in BTHS and is found in 100% of affected individuals (6) .

BTHS is a multisystem disorder characterized by prenatal onset of left ventricular noncompaction, early onset cardiomyopathy, skeletal myopathy, growth abnormalities, and neutropenia among other features, and is the only known Mendelian disorder of CL metabolism (1, 7–9). Despite knowledge of the primary metabolic defect in BTHS, there is limited knowledge of downstream mechanisms of cellular pathogenesis, and consequently there is a dearth of targets for therapeutic intervention and clinical monitoring (10). In addition to BTHS, CL abnormalities have been described in common conditions such as idiopathic cardiomyopathy, fatty liver disease, and diabetes (1, 11–14). Consequently, studies in BTHS have the potential to illuminate pathophysiology in a range of common diseases.

To identify novel and unappreciated cellular pathways impacted by TAZ deficiency we employed a discovery-based approach in a new HEK293 TAZ-deficient cellular model, starting with untargeted proteomics followed by functional analysis, and validation of pathways of interest in both HEK293 TAZ-deficient cells and patient derived lymphoblastoid cell lines (LCLs). With this approach we characterized two major areas of dysfunction in the inner mitochondrial membrane: complex I (CI) of the mitochondrial respiratory chain and mitochondrial quality control (MQC).

Prior studies seeking to define the mitochondrial pathology of TAZ deficiency have described abnormal assembly and function of the mitochondrial respiratory complexes (15–17). In agreement with these findings, we identified aberrations in mitochondrial respiratory chain protein abundance and enzymatic function, specifically in CI. Significantly, our findings show that TAZ deficiency results in the reduced CI mRNA expression with evidence for distinct regulation in differing cell types.

3

88   In addition to expanding our current understanding of respiratory chain abnormalities in

89   TAZ deficiency, we also identified novel abnormalities in regulators of MQC. We uncovered

90   aberrant abundance of the MQC protein, mature mitochondrial PARL, which was accompanied

91   by altered cleavage of the downstream MQC mediator and PARL target, PGAM5. PGAM5

92   cleavage abnormalities were further amplified by uncoupling of mitochondrial oxidative

93   phosphorylation, suggesting that baseline MQC abnormalities in TAZ-deficient cells can be

94   exacerbated with additional stress.

95   Finally, we found that modulating CL normalizes gene expression of CI subunits,

96   normalizes the abundance of CI holoenzyme, and remediates the aberrant ratio of cleaved to

97   full length PGAM5. Thus, abnormal CL in TAZ deficiency has a direct role in dysregulating both

98   CI of the mitochondrial respiratory chain and MQC.

99

100   **Results**

101   **Generation of a HEK293 TAZ-KO model, $TAZ^{\Delta 45}$**

102   We used CRISPR/Cas9 genome editing in HEK293s to create a novel TAZ-deficient cellular

103   model. Using two single guide RNAs (sgRNAs) targeting exon 2 of *TAZ*, we isolated 3 individual

104   clones with a resultant 45bp deletion at the 3'- end of exon 2; $TAZ^{\Delta 45.4}$, $TAZ^{\Delta 45.5}$, $TAZ^{\Delta 45.6}$ (Fig.

105   S1). The deletion encompasses a predicted acyltransferase domain and covers an area of *TAZ*

106   where multiple pathological variants have been described, such as p.R57L and p.H69Q (Fig.

107   S1) (3). The 45bp in-frame deletion is not predicted to result in NMD (Fig. 1A). However, the

108   deletion resulted in undetectable expression of TAZ in all three clones (Fig. 1B). In the absence

109   of TAZ there was no significant difference in the abundance of cytosolic and mitochondrial

110   proteins/immunoblotting controls; GRP75, ß-actin, VDAC1, and TOM20 (Fig. S2).

111   Shotgun lipidomics via mass spectrometry revealed a significant decrease in CL, a

112   significant increase in MLCL, and a significantly increased MLCL:CL ratio (p=0.03, p=4.9 x 10^{-5},

113   p=4.6 x 10^{-6}, respectively) (Fig. 1C). TAZ-based remodeling is characterized by the

114   incorporation of unsaturated acyl chains compared to nascent CL. Of the 31 CL species

115   assessed, the $TAZ^{\Delta 45}$ clones had a significant increase in CL containing 1 to 3 double bonds

116   (p=0.007, p=1.5 x 10^{-9}, p=7.4 x 10^{-6}, respectively) and a significant decrease in CL containing 4

117   to 6 double bonds (p=0.03, p=0.003, p=4.2 x 10^{-9}, respectively), highlighting the loss of TAZ-

118   based remodeling (Fig. 1D). Collectively, the $TAZ^{\Delta 45}$ clones recapitulate the pathognomonic

119   metabolic defect of BTHS and validate the $TAZ^{\Delta 45}$ clones as TAZ-deficient cellular models of

120   BTHS.

4

121   We were able to amplify and Sanger sequence 5 of the top 10 predicted off-target sites,

122   5 off-target sites per sgRNA, which revealed no detectable off-target CRISPR/Cas9 genome

123   editing activity (Table S1). The other 5 off-target sequences were not able to be amplified likely

124   due to highly repetitive sequences and/or increased GC base pair content. None of the top 10

125   predicted off-target sites were located in coding regions. In order to mitigate consequences of

126   undetected off-target editing in any one of the clones, the clones, $TAZ^{\Delta 45.4}$, $TAZ^{\Delta 45.5}$, $TAZ^{\Delta 45.6}$,

127   were combined at a 1:1:1 ratio to create the cellular model $TAZ^{\Delta 45}$.

128   **Differentially abundant proteins in $TAZ^{\Delta 45}$ cells reveal downstream cellular dysfunction**

129   **due to TAZ deficiency**

130   Shotgun proteomics analysis identified a total of 7713 proteins in HEK293 WT and $TAZ^{\Delta 45}$ cells.

131   To focus our downstream workflow on proteins with differential abundance between the WT and

132    $TAZ^{\Delta 45}$ cells, we selected proteins with a protein abundance fold change (FC, $TAZ^{\Delta 45}$/ WT) less

133   than or equal to 0.80 (FC ≤ 0.80) and proteins with a FC greater than or equal to 1.2 (FC ≥ 1.20)

134   (Fig. 1E). Based on these criteria, there were a total of 836 differentially abundant proteins, 215

135   with a FC ≤ 0.80 and 621 with a FC ≥ 1.20 (Fig. 1E). Functional annotation of the differentially

136   abundant proteins, with KEGG pathway and gene ontology (GO) term enrichment analysis,

137   identified multiple pathways of interest in $TAZ^{\Delta 45}$ cells (Table S2A-B) (18, 19).

138   We identified 86 significantly enriched (p ≤ 0.05) KEGG pathways and GO terms for

139   proteins with a FC ≤ 0.80, such as: oxidative phosphorylation (p=2.7 x 10^{-6}), mitochondrial

140   respiratory chain complex I assembly (p=7.9 x 10^{-5}), mitochondrial chain complex I (p= 2.1 x 10^{-4}

141   ^{4}), response to oxidative stress (p=1.6 x 10^{-3}), NADH dehydrogenase (ubiquinone) activity

142   (p=2.1 x 10^{-3}), and metabolic pathways (p=0.019) (Table S2A). We identified 127 significantly

143   enriched (p ≤ 0.05) KEGG pathways and GO terms for proteins with a FC ≥ 1.20, such as:

144   mitochondrion (p=2.2 x 10^{-4}), metabolic pathways (p=3.1 x 10^{-3}), positive regulation of apoptotic

145   process (p=4.2 x 10^{-3}), AMPK signaling pathway (p=7.5 x 10^{-3}), response to oxidative stress

146   (p=9.3 x 10^{-3}) (Table S2B).

147   **Functional annotation analysis: proteins of respiratory complex I and mitochondrial**

148   **quality control**

149   Defects in OXPHOS function have been previously described in BTHS, and consistent

150   with these previous studies, we found that of the 86 terms significantly enriched for proteins with

151   FC ≤ 0.80 in $TAZ^{\Delta 45}$ cells, 18 reference the mitochondrion and/or OXPHOS, including the

152   OXPHOS KEGG pathway (Table S2A). Specifically, 11 proteins with a FC ≤ 0.80 are encoded

153   by genes associated with the OXPHOS KEGG pathway (Fig. S3). Of these 11 proteins, 5 are

154   subunits of complex I (CI) and the remaining 6 proteins are subunits of complex III, IV, and V

155 (Fig. S3). When we further examined the 18 terms that reference the mitochondrion and/or

156 OXPHOS, we found that 4 specifically reference CI of OXPHOS (Table S2A).

157 The enrichment of the CI-associated terms in our functional annotation analysis was

158 driven by 7 proteins encoded by the genes: *MT-ND3, NDUFAF1, NDUFA5, NDUFAB1,*

159 *NDUFB2, NDUFB4,* and *OXA1L* (Fig. 2A). Five are subunits of CI (*MT-ND3, NDUFA5,*

160 *NDUFAB1, NDUFB2, NDUFB4*), one is a CI assembly factor (*NDUFAF1*), and one assists with

161 inserting proteins into the mitochondrial membrane and has been implicated in CI biogenesis

162 (*OXA1L*) (20, 21). In total, proteomics identified and quantified 56 CI associated proteins in WT

163 and *TAZ^{\Delta45}* cells, and 45/56 had reduced abundance in *TAZ^{\Delta45}* cells (FC range=0.608-0.998)

164 (Table S3). Together, the functional annotation analysis highlights a decreased abundance of

165 proteins associated with complex I, further delineating a previously described pathway in BTHS.

166 When we analyzed the top five proteins with significantly increased abundance, we

167 identified PARL as a candidate for further study due to its role in regulating mitochondrial

168 responses to stress, such as membrane depolarization and increased reactive oxygen species

169 (22–24). Additionally, dysregulation of PARL substrates has been implicated in cardiomyopathy

170 and cardiac development, further highlighting the potential role of PARL dysregulation in BTHS

171 (25–27). Upon further investigation of the 127 terms significantly enriched for proteins with a FC

172 > 1.20, we observed that 20 terms reference the mitochondrion or mitochondrial dynamics,

173 including: metabolic pathways (p=3.1 x 10^{-3}), positive regulation of the apoptotic process (p=4.2

174 x 10^{-3}), and mitochondrial inner membrane (p=5.2 x 10^{-3}) (Table S2B). The functional annotation

175 analysis revealed other genes of interest due to their potential roles in apoptosis, lipid trafficking,

176 and/or mitochondrial quality control (MQC), such as; PRELID1, PRELID3B, CASP2, CASP7,

177 CASP8, and CASP9 (28–30). Together with the proteomics findings, the functional annotation

178 analysis suggests an increased abundance of proteins involved in MQC, a pathway not

179 previously described in BTHS.

180 **Reduced complex I holoenzyme and activity in HEK293 *TAZ^{\Delta45}* cells and BTHS patient**

181 **derived lymphoblastoid cells**

182 To assess the biological significance of reduced CI associated proteins identified via

183 proteomics, we further investigated CI subunit/holoenzyme mRNA expression, protein

184 abundance, and function. We measured the relative mRNA expression of *NDUFAF1*, the most

185 significantly reduced protein identified by proteomics (FC=0.797, p=0.004), in both HEK293 and

186 BTHS patient derived lymphoblastoid cells (LCLs). In *TAZ^{\Delta45}* cells, *NDUFAF1* had reduced

187 mRNA expression (0.80, p=6.4 x 10^{-4}), whereas in BTHS LCLs there was no significant

188 difference in mRNA expression (Fig. 2B).

6

189   We also measured the relative mRNA expression the 5 other CI associated proteins that

190   had a FC ≤ 0.80 (MT-ND3, NDUFA5, NDUFB2, NDUFAB1, and NDUFB4), as well as 3

191   additional CI associated proteins (NDUFA9, NDUFS3, and NDUFB6), which did not have a FC

192   ≤ 0.80 but had been previously shown to have reduced protein abundance in BTHS LCLs (Fig.

193   2A & Fig. S4) (17). Of these 8 genes, 4 had significantly reduced mRNA expression in $TAZ^{\Delta45}$

194   cells (*NDUFB2* p=0.04, *NDUFAB1* p=0.001, *NDUFB4* p=0.02, and *NDUFB6* p=0.01) (Fig. S4).

195   *NDUFA5, NDUFA9,* and *NDUFS3* had reduced mRNA expression in $TAZ^{\Delta45}$ cells but this

196   reduction did not reach statistical significance (Fig. S4). There were no significant differences in

197   the mRNA expression between control and BTHS LCLs, however there was significant

198   variability in mRNA expression of all genes between the 5 individual BTHS LCL lines (Fig. S5).

199   These individual differences could be due to the individual patient's genetic background or the

200   EBV transformation of the LCLs and may obfuscate the biological significance of mRNA

201   expression in patient-derived LCLs.

202   Immunoblotting of HEK293 and LCL whole cell lysate for NDUFAF1 confirmed reduced

203   protein abundance in $TAZ^{\Delta45}$ cells (FC=0.69, p=4.89 x 10^{-10}) and BTHS LCLs (FC=0.75, p=7.69

204   x 10^{-7}) (Fig. 2C). We also immunoblotted HEK293 and LCL mitochondria for the 3 additional CI

205   subunits that had been previously shown to have reduced protein abundance (17). There was a

206   subtle trend towards reduced NDUFA9, NDUFS3, and NDUFB6 abundance in $TAZ^{\Delta45}$ cells

207   (p=ns, p=0.04, p=0.05, respectively), and a strong reduction in BTHS LCLs (p=7.6 x 10^{-6}, p=1.8

208   x 10^{-7}, p=5.1 x 10^{-6}, respectively) (Fig. S6). The abundance of NDUFA9, NDUFS3, and NDUFB6

209   in $TAZ^{\Delta45}$ cells aligns with our proteomics findings, that found no significant difference in the

210   abundance of these proteins between WT and $TAZ^{\Delta45}$ cells (Fig. 2A, Fig. S6). In order to

211   determine whether TAZ deficiency affected the protein abundance of subunits from other

212   respiratory complexes, we also immunoblotted for UQCRC2, a subunit of respiratory complex

213   III. We found no significant difference in UQCRC2 abundance between WT and $TAZ^{\Delta45}$ cells,

214   and a subtle but significantly reduced abundance of UQCRC2 in BTHS LCLs compared to

215   controls (Fig. S6).

216   To determine the total abundance of CI holoenzyme, HEK293 and LCL cells were

217   solubilized with Triton X-100 and resolved by BN-PAGE for the quantification of individual

218   respiratory complexes. CI was the most significantly reduced complex, and the ratio of CI to CIV

219   (CI:CIV) or CI:CII was significantly reduced in both $TAZ^{\Delta45}$ vs. WT (p=2.32 x 10^{-5}, p=1.62 x 10^{-4},

220   respectively) and BTHS LCLs vs. controls (p=0.001, p=0.005, respectively) (Fig. 2D). By

221   comparing starting material and the cellular pellet following solubilization via immunoblotting, we

222   found no significant difference in the solubilization of $TAZ^{\Delta 45}$ and WT cells (87% and 88%

223   solubilization efficiency, respectively). There was a minimal though statistically significant

224   difference in the solubilization of BTHS and control LCLs (84% and 79% solubilization

225   efficiency, respectively, p=0.03). Therefore, the observed differences were not due to an effect

226   of altered CL on Triton X-100 solubilization.

227   Using a colorimetric CI enzyme activity assay that detects the oxidation of NADH to

228   NAD^+, we found a significant reduction in CI activity in both $TAZ^{\Delta 45}$ cells and BTHS LCLs (p=9.4

229   x 10^{-5} & p=1.8 x 10^{-4}, respectively) (Fig. 2E). Using a colorimetric CII enzyme activity assay, we

230   found no significant difference in CII activity between WT and $TAZ^{\Delta 45}$ cells or between control

231   and BTHS LCLs, emphasizing the preeminent role of CI in BTHS-associated OXPHOS

232   dysfunction (Fig. 2F). There was a wide range of CII function in LCLs derived from different

233   individuals (Fig. S7). Overexpression of NDUFAF1, a CI assembly factor and the most

234   significantly reduced CI associated protein in $TAZ^{\Delta 45}$ cells, did not normalize the CI functional

235   deficiency in $TAZ^{\Delta 45}$ cells, indicating that CI dysfunction is due to a combination of reduced

236   subunits and assembly factors (Fig. S8).

237   Measurement of intracellular NADH and NAD+ showed a trend towards an increase in

238   the ratio of NADH to NAD^+ in both $TAZ^{\Delta 45}$ and BTHS LCLs compared to either WT or controls,

239   though neither reached statistical significance (Fig. 2G). There was also an increase in

240   intracellular AMP in both $TAZ^{\Delta 45}$ cells and BTHS LCLs compared to either WT or controls, with a

241   significant increase in the BTHS LCLs (p=0.002) (Fig. 2H). This moderate disturbance in energy

242   homeostasis is consistent with the modest perturbations we observed in CI from mRNA

243   expression, to protein expression, and ultimately activity in TAZ-deficient cells.

244   **Increased PARL abundance correlates with increased cleavage of downstream target**

245   **PGAM5**

246   To confirm the proteomics finding of increased PARL abundance (FC=1.815, p=0.016) in TAZ-

247   deficient HEK293 cells, we immunoblotted HEK293 and LCL whole cell lysate for PARL. Using

248   a PARL-KO HEK293 cell line generously provided by the Langer Laboratory, we identified a

249   single band at ~33kD present in both WT and $TAZ^{\Delta 45}$ cells and absent in the PARL-KO cells,

250   consistent with the band representing mature mitochondrial PARL (MAMP-PARL), referred to as

251   PARL (Fig. S9) (24).

252   In $TAZ^{\Delta 45}$ cells there was a significant increase in the abundance of PARL (FC=1.51,

253   p=1.81 x 10^{-10}) (Fig. 3A). There was a subtle but significant increase in the relative mRNA

254   expression of PARL in $TAZ^{\Delta 45}$ cells (WT=0.97, $TAZ^{\Delta 45}$=1.09, p=0.02) (Fig. 3B). Immunoblotting

255   of LCL whole cell lysate for PARL showed a significant reduction in PARL abundance, however,

256   there was extreme variability in PARL abundance in the CTRL lines (CTRL 1-3 vs CTRL 4-5)

257   (Fig. S10A). There was no significant difference in the mRNA expression of PARL between

258   CTRL and BTHS LCLs or across the 5 different BTHS LCL lines (Fig. S10B-C). Thus, increased

259   PARL in TAZ-deficient HEK293 cells may be regulated both at the transcriptional and protein

260   expression levels, and lack of consistent findings in BTHS LCLs may be due to cell-type specific

261   differences in PARL regulation or difficulty with detection in a small sample size due to high

262   intra-subject variability.

263   To investigate the biological significance of increased PARL abundance in $TAZ^{\Delta 45}$ cells,

264   we assessed a downstream proteolytic target of PARL, PGAM5. Previous evidence suggests

265   that PGAM5 is cleaved by PARL and another stress-activated IMM protease, OMA1, in

266   response to loss of mitochondrial membrane potential ($\Delta\Psi_m$) (31). At baseline, we observed a

267   significant increase in the percent of cleaved PGAM5 in $TAZ^{\Delta 45}$ cells ($p=1.5 \times 10^{-7}$) (Fig. 3C).

268   There was no significant difference in the percent of cleaved PGAM5 between CTRL and BTHS

269   LCLs (Fig. S10D)

270   Upon treatment with membrane depolarizer carbonyl cyanide m-chlorophenyl hydrazine

271   (CCCP), with serial time point measurements, we observed that $TAZ^{\Delta 45}$ cells maintained a

272   significantly greater abundance of PARL until the final timepoint of 120 mins (Fig. 3E, Table S5).

273   This increase in PARL abundance with CCCP correlates with the increase in PGAM5 cleavage

274   observed in both WT and $TAZ^{\Delta 45}$ cells (Fig. 3D). Under the same CCCP treatment protocol, we

275   also observed an increase in the percentage of cleaved PGAM5 in WT cells and $TAZ^{\Delta 45}$ cells,

276   where $TAZ^{\Delta 45}$ cells maintained a significantly greater percentage of cleaved PGAM5 at all time

277   points tested (Fig. 3D). The difference in the percentage of cleaved PGAM5 between WT and

278   $TAZ^{\Delta 45}$ cells increased over time, from a 11% difference at 0 mins to a 18% difference at 120

279   mins (Fig. 3D, Table S4).

280   We further demonstrated that PGAM5 cleavage was absent and reduced inn PARL-KO

281   cells not treated or treated with CCCP, respectively, underscoring that PGAM5 is predominantly

282   cleaved by PARL (Fig. 3F). In summary, we observed baseline abnormalities in PARL

283   abundance and PGAM5 cleavage, which is exacerbated upon mitochondrial depolarization, in

284   TAZ-knockout HEK293 cells.

285   **Targeting CL with bromoenol lactone and SS-31 normalizes downstream cellular**

286   **dysfunction**

287   To determine if targeting CL and CL metabolism would affect the dysregulation observed

288   in respiratory CI and/or MQC, $TAZ^{\Delta45}$ and WT cells were treated with either bromoenol lactone

289   (BEL) or SS-31. Previous studies have shown that treatment with BEL, an inhibitor of calcium-

290   independent PLA_2 ($iPLA_2$), partially remediates CL abnormalities by reducing MLCL

291   accumulation and CL depletion (32, 33). SS-31, a cell permeable mitochondria-targeted

292   tetrapeptide, selectively binds CL where it has been shown to stabilize cristae morphology and

293   preserve mitochondrial bioenergetics (34, 35).

294   The relative abundance of NDUFAF1 in $TAZ^{\Delta45}$ cells increased following BEL treatment

295   and significantly increased following SS-31 treatment (p= 2.8 x 10^{-5}) (Fig. 4A, Table S6).

296    $NDUFAF1$ relative mRNA expression significantly increased in $TAZ^{\Delta45}$ cells following both BEL

297   and SS-31 treatment (p= 0.05 and p= 0.01, respectively) (Fig. 4B, Table S7). The relative

298   mRNA expression was also measured for the other 4 CI associated genes that had significantly

299   reduced levels in $TAZ^{\Delta45}$ cells at baseline ($NDUFB2$, $NDUFAB1$, $NDUFB4$, and $NDUFB6$).

300   Following BEL treatment, these significant differences in expression between $TAZ^{\Delta45}$ vs. WT

301   were no longer observed in any of the 4 genes tested, and following SS-31 treatment, the

302   significant differences were no longer observed in 3 of the 4 genes tested (Fig. S12, Table S7).

303   Next, CI holoenzyme abundance was measured in BEL and SS-31 treated cells by BN-

304   PAGE. CI remained the most significantly reduced complex in $TAZ^{\Delta45}$ cells after BEL or SS-31

305   treatment (Fig. 4C). However, both treatments had a subtle effect on the ratio of both CI to CIV

306   (CI:CIV) and CI to CII (CI:CII) (Fig. 4C, Table S8). The CI:CIV relative abundance increased

307   from 0.59 in untreated $TAZ^{\Delta45}$ cells to 0.77 in $TAZ^{\Delta45}$-BEL cells and 0.80 in $TAZ^{\Delta45}$-SS-31 cells

308   (Fig. 4C, Table S8). The CI:CII relative abundance significantly increased from 0.66 in untreated

309    $TAZ^{\Delta45}$ cells to 0.89 in $TAZ^{\Delta45}$-BEL cells (p= 6.1 x 10^{-3}) and to 0.83 in $TAZ^{\Delta45}$-SS-31 cells (Fig.

310   4C, Table S8). Overall, treatment with either BEL or SS-31 showed a subtle increase in CI

311   holoenzyme abundance.

312   Immunoblotting of BEL and SS-31 treated HEK293 whole cell lysate for PGAM5 showed

313   a significant decrease in the percentage of cleaved PGAM5 in $TAZ^{\Delta45}$-BEL (18%, p= 0.01) and

314    $TAZ^{\Delta45}$-SS-31 (13%, p= 2.6 x 10^{-4}) cells compared to $TAZ^{\Delta45}$-untreated cells (23%) (Fig. 4D,

315   Table S9). There was no significant difference in the percentage of cleaved PGAM5 in $TAZ^{\Delta45}$-

316   BEL versus WT-BEL cells or $TAZ^{\Delta45}$-SS-31 versus WT-SS-31 cells (Fig. 4D, Table S9). Further,

317   immunoblotting of BEL and SS-31 treated HEK293 whole cell lysate for PARL showed a

318   significant decrease in the relative abundance of PARL in $TAZ^{\Delta45}$-BEL (FC= 0.93, p= 7.1 x 10^{-15})

319   and $TAZ^{\Delta45}$-SS-31 (FC= 1.11, p= 9.9 x 10^{-5}) cells compared to $TAZ^{\Delta45}$-untreated cells (FC= 1.53)

10

320   (Fig. 4E, Table S10), which was essentially restored to WT levels. Collectively, these results

321   indicate that drugs that target CL partially rescue the defects in CI and MQC observed in TAZ-

322   deficient cells.

323

324   **Discussion**

325   As a central phospholipid of the IMM, CL has been shown to have diverse roles in mitochondrial

326   function (1). Yet, these diverse roles are currently underappreciated in the pathophysiology of

327   Barth syndrome, which is the only known Mendelian disorder of CL metabolism. In this study,

328   we took an untargeted approach to identify dysregulated proteins in TAZ-deficient HEK293 cells

329   and pursued two areas of dysregulation for further study: CI of the respiratory chain and

330   components of mitochondrial quality control.

331   Previous work has linked TAZ deficiency and mitochondrial respiratory chain

332   dysfunction, with several studies pointing towards CI as the most impacted respiratory chain

333   complex (15, 17, 36). In this work we confirmed that CI expression and function are abnormal in

334   TAZ deficiency. We further showed that this dysfunction is potentially driven by the decreased

335   expression of 5 subunits of mitochondrial CI, *MT-ND3*, *NDUFA5*, *NDUFAB1*, *NDUFB2*,

336   *NDUFB4,* and reduced expression of the mitochondrial assembly factor, *NDUFAF1*. These

337   specific deficiencies could disrupt aspects of the coordinated modular assembly of CI and

338   further studies into CI modular assembly in BTHS could prove to be revealing (20, 37).

339   We further identified abnormal expression and regulation of MQC associated proteins

340   including PARL and PGAM5. MQC, involving the processes of mitochondrial proteostasis,

341   biogenesis, dynamics, and mitophagy, is emerging as a central theme for the pathogenesis of

342   various diseases (38–40). PARL participates in MQC via reciprocal proteolysis of PGAM5 and

343   PINK1 (22, 31). Upon mitochondrial depolarization, PARL upregulation accelerates PGAM5

344   proteolysis which drives mitochondrial fragmentation (31). Defective mitochondrial quality

345   control, particularly as it affects cellular energy production and stress responsiveness, is

346   increasingly recognized for its role in diverse forms of cardiac dysfunction and may be central to

347   the cardiac pathogenesis of BTHS (41).

348   In order to determine if the abnormalities we identified are directly associated with

349   abnormal CL, we tested the ability of a pharmacological inhibitor of PLA2γ (BEL), a protein

350   capable of generating MLCL from CL, and a CL binding peptide (SS-31) to ameliorate the two

351   TAZ-deficient phenotypes we established. Indeed, we showed that targeting CL and CL

352   metabolism with BEL and SS-31 is sufficient to modulate CI subunit gene expression and

11

353   protein abundance, PARL abundance, and PGAM5 cleavage. Thus, targeting multiple aspects

354   of CL metabolism may be a feasible therapeutic approach in BTHS.

355   In terms of future directions for study, it is notable that among the CI subunits that we

356   identified as having altered expression in TAZ deficiency, NDUFAB1 has an essential role in

357   fatty acid biosynthesis due to its dual role as the mitochondrial acyl carrier protein (mt-ACP)

358   (42). In fact, the GO term "protein lipoylation" was identified in the functional annotation of

359   proteins with a FC ≤ 0.80 (Table S2A). In this role, abnormal expression of NDUFAB1/mt-ACP

360   in TAZ deficiency may have further implications beyond affecting CI assembly and function,

361   including affecting CL acyl chain content. Additionally, mt-ACP is involved in the assembly of the

362   mitochondrial ribosome, and therefore mt-ACP expression and abundance may further influence

363   changes in mitochondrial gene expression (43). Further examining the essential role of

364   NDUFAB1, outside of CI assembly and function, may provide a mechanistic link between

365   altered CL metabolism and altered bioenergetic metabolism. Defects in MQC pathways, have

366   been implicated in the pathogenesis of various cardiac pathologies relevant to BTHS.

367   Additionally, enlarged mitochondria have been observed in BTHS patient and mouse model

368   derived cardiac tissue, consistent with impaired mitophagy (44–47). Thus, further examining

369   these pathways in an appropriate cellular context could provide insight into potential therapeutic

370   targets for BTHS and other conditions resulting from MQC dysfunction.

371   Finally, it is important to note that some of our findings were cell-type specific (HEK293

372   vs. LCL). We found that HEK293s and LCLs differed in PARL abundance, which is consistent

373   with previous studies confirming cell-type specific expression and regulation of PARL, and

374   introduces further questions about whether cell-type specific mechanisms of MQC contribute to

375   the tissue distribution of disease in BTHS (48). We also identified a reduction in CI subunit

376   protein abundance, holoenzyme abundance, and CI activity in both HEK293 TAZ-KO cells and

377   BTHS LCLs; however, in BTHS LCLs reduced mRNA expression of CI subunits was not

378   observed. The differences in mRNA expression observed between the HEK293s and the LCLs

379   could be due to epigenetic and transcriptomic differences observed in EBV transformed LCL

380   lines, the genetic differences between the BTHS individuals, and/or cell type specific regulation

381   of CI associated genes/proteins (49). This hypothesis emphasizes the need for a clearer

382   understanding of the cell-specific effects of abnormal CL content. To explore these questions,

383   we are presently exploring respiratory chain and MQC dysfunction in diverse TAZ-KO cell types

384   in order to understand how these pathways are associated with the tissue specific expression of

385   BTHS.

386

387 **Materials and Methods**

388 **Cell lines and culture conditions.**

389 HEK293 WT cells were purchased from ATCC (293 [HEK-293]x ATCC® CRL-1573™).

390 Collection of control (LCL Control #1) and BTHS patient (LCL BTHS #1-5) derived LCL lines

391 had institutional IRB approval via Johns Hopkins University protocols #IRB00098987 (Table

392 S11). Individuals were diagnosed with BTHS via an increased MLCL:CL ratio. Additional control

393 LCL lines (n=9) were acquired through the following sources: Biochemical Genetics Laboratory

394 at Kennedy Krieger Institute (LCL Control #2-3), Valle Laboratory (LCL Control #4-5), Coriell

395 NINDS Biobank (LCL Control #6-9) (Table S11).

396 LCL lines were transformed by the Biochemical Genetics Laboratory at Kennedy Krieger

397 Institute and the Valle Laboratory used the following protocol. Peripheral blood samples were

398 centrifuged for 15 minutes at 3000 rpm. The "buffy coat" was then resuspended in RPMI and

399 further centrifuged for 10 minutes at 1000 rpm. The resulting cell pellet was resuspended in

400 RPMI and incubated with Epstein-Barr (EB) virus and T-cell growth factor (TCGF) at 37C for 48-

401 72 hours. After incubation period, additional RPMI was added to the flask. Cells were monitored

402 and fed RMPI for two weeks, after which the established transformed cell lines were passaged

403 for experiments and/or freezing. LCL lines acquired through the Coriell NINDS Biobank were

404 also transformed via EB virus.

405 All cells were grown at 37°C, 5% CO2. HEK293 WT and TAZ$^{\Delta 45}$ were maintained in

406 DMEM with L-glutamine and 4.5 g/L Glucose (Corning Cellgro Cat. #10-017) containing 10%

407 fetal bovine serum (FBS, Gemini) and 2 mM L-glutamine (Gibco, Cat. #25030149). Patient

408 derived lymphoblastoid cells (LCLs) were maintained in RPMI 1640 (Gibco, Cat. # 11875119)

409 containing 10% FBS (Gemini). Mycoplasma contamination was routinely monitored and not

410 detected.

411 For CCCP treatment, HEK293s were seeded into 6-well plates. At confluence, cells were

412 either treated with 20uM CCCP (Cat. No) for 0,10,30,60,90, and 120 mins, or

413 0,10,20,40,80,100uM CCCP for 45 mins.

414 For BEL treatment, HEK293s (400K) were seeded into 6-well plates. 48hrs later, at 80-

415 90% confluence, cells were treated with 2.5uM BEL (Cat. No) for 48hrs.

416 For SS-31 treatment, HEK293s (50K) were seeded into 6-well plates. For 7 days, cells

417 were fed fresh 100nM SS-31.

418 **CRISPR/Cas9 genome editing**

419 sgRNAs (Figure S1 & Table SI) targeting exon 2 of *TAZ* were designed at www.crispr.mit.edu

420 and selected based on the scoring algorithm detail in Hsu et al. 2013 (Table S1) (50, 51).

13

421   Synthesized sgRNA 1 and sgRNA 2 were individually cloned into pSpCas9(BB)-2A-Puro

422   (PX459) V2.0 vector pSpCas9(BB)-2A-Puro (PX459) V2.0 was a gift from Feng Zhang

423   (Addgene plasmid # 62988 ; http://n2t.net/addgene:62988 ; RRID:Addgene_62988 (50).

424   HEK293 WT cells were transfected with both sgRNA vectors using Lipofectamine 2000

425   (Invitrogen). 24-hours after transfection cells were subjected to Puromycin selection (2ug/mL)

426   for approximately 48 hours. Following selection, cells we passaged in order to isolate single cell

427   clones. Confluent colonies of single cell clones were collected using a cloning cylinder and

428   expanded for DNA isolation and screening.

429   **Screening and genotyping**

430   Genomic DNA was extracted from an aliquot of 3×10^6 cells using the Gentra Purgene Kit

431   (Qiagen). The genomic region surrounding the CRISPR/Cas9 target site (741 bp) was PCR

432   amplified using AccuPrime GC-Rich DNA Polymerase (Invitrogen) (Table S1). The PCR product

433   was then used for screening with Surveyor Assay Kit (IDT). The PCR product of Surveyor-

434   Positive clones was further analyzed by Sanger sequencing.

435   **RT-PCR**

436   RNA was extracted from an aliquot of 3×10^6 cells using the RNeasy Plus Kit (Qiagen). cDNA

437   was synthesized from extracted RNA using the iScript cDNA Synthesis Kit (BioRad). The region

438   surrounding the CRISPR/Cas9 target site was PCR amplified using AccuPrime GC-Rich DNA

439   Polymerase (Invitrogen) (Forward Primer: 5' TACATGAACCACCTGACCGT 3', Reverse Primer:

440   5' CAGATGTGGCGGAGTTTCAG 3'). PCR products were resolved on a 0.8% agarose gel.

441   **Whole Cell Lysate Extraction**

442   An aliquot of 3×10^6 cells was centrifuged for 4 minutes at 1000rpm. The resultant cell pellet

443   washed twice with ice-cold PBS and lysed with RIPA lysis buffer (1% (v/v) Triton X-100, 20 mm

444   HEPES–KOH, pH 7.4, 50 mm NaCl, 1 mm EDTA, 2.5 mm $MgCl_2$, 0.1% (w/v) SDS) spiked with

445   1 mm PMSF for 30 min at 4°C with rotation. Insoluble material was removed by centrifugation

446   for 30 min at 21000g at 4°C, the supernatant collected, and protein quantified using a

447   bichichronic acid (BCA) assay (Pierce).

448   **Mitochondrial Isolation**

449   Mitochondrial isolation of HEK293s was performed as previously described by Lu et al.(3).

450   Mitochondrial isolation of LCLs was also performed as previously described, with slight

451   modification. LCLs were grown in maintenance media until total cell count exceeded 100×10^6

452   cells. LCLs were then centrifuged for 4 minutes at 1000rpm before beginning the previously

453   described protocol by Lu et al.(3).

454   **Immunoblotting**

14

455   Whole cell extracts or mitochondria, resuspended in XT Sample Buffer (BioRad) and Reducing

456   Agent (BioRad), were resolved on Criterion XT 12% Bis-Tris gels (BioRad) in XT MOPS

457   Running buffer (BioRad). Proteins were transferred to Immuno-Blot PVDF (BioRad) at 100V for

458   1 hour. Following transfer, membranes were blocked with 5% milk, 0.05% Tween-20 in PBS

459   (Blocking Buffer) for 1 hour at room temperature or at 4C if longer, with rocking. Following

460   blocking, membranes were briefly washed with PBST (PBS with 0.2% Tween-20) and then

461   incubated with primary antibody in PBST with 0.02% Na-Azide overnight at 4C with rocking.

462   Following three successive 10-minute washes with PBST at room temperature, HRP-conjugated

463   secondary antibodies were added and incubated for 45 min at room temperature. The

464   membranes were then washed three times for 10 minutes with PBST and twice for 10 minutes

465   with PBS. Immunoreactive bands were visualized using ECL Western Blotting Detection

466   (Amersham) or SuperSignal West Pico PLUS (Pierce). Images were captured with a Fluorchem

467   Q (Cell Biosciences, Inc.) or on film. Film was scanned before quantification. Quantitation of

468   bands was performed using ImageJ and protein expression values were normalized to loading

469   controls.

470   **Antibodies**

471   Antibodies against the following proteins were used; β-actin (loading control, Life Technologies

472   #AM4302), GRP75 (loading control, 75-127), TAZ (#2C2C9)(3), NDUFAF1 (Abcam, #ab79826),

473   PARL (Abcam #ab45231, Proteintech #26679-1-AP, Langer Laboratory), UQCRC2 (Abcam,

474   #ab14745), NDUFA9 (Abcam, #ab14713), NDUFS3 (Abcam, #ab110246), NDUFB6 (Abcam,

475   #ab110244). Two HRP-conjugated secondary antibodies were used; goat anti-rabbit (Abcam,

476   #ab6721), goat anti-mouse (Abcam, #ab205719).

477   **Lipidomics**

478   Lipids were extracted from cell pellets (3 x 10^6 cells) and analyzed as previously described by

479   Vaz et al. (52).

480   **Proteomics**

481   Samples (HEK293 WT n=3, and TAZ$^{\Delta 45}$ n=3, serial passages) were reduced in 5 mM DTT for 1

482   hour at 56C, alkylated in 10 mM iodoacetamide for 30 minutes in the dark at room temperature,

483   and precipitated in cold (-20C) acetone 10% trichloroacetic acid. The precipitate was pelleted by

484   centrifugation at 16,000 g for 15 minutes, the supernatant was discarded, and the pellet was

485   rinsed with cold acetone and dried at room temperature. The samples were reconstituted in 50

486   µL of 20% acetonitrile 80 mM triethyl ammonium bicarbonate (TEAB) and digested with 3.3 µg

487   of trypsin/Lys-C mix (Promega) at 37C overnight. The digested samples were labeled with TMT

488   10-plex reagent (Thermo, Lot #SK257889) and combined. The sample was lyophilized and

489   reconstituted in 0.5 mL of 10 mM TEAB and fractionated by high (8-9) pH reversed phase

490   chromatography into 84 fractions which were concatenated into 24. Each of the 24 fractions was

491   lyophilized and reconstituted in 2% acetonitrile 0.1% formic acid and separated over a 90-

492   minute low (2-3) pH reversed phase gradient (120 minutes run time) for mass spectrometry

493   (MS) analysis on an Orbitrap Fusion.

494   MS data were acquired using serial data-dependent fragmentation of individual

495   precursor ions (DDA). An intact precursor ion scan (MS1) spanning 400 - 1600 Th was acquired

496   every 3 seconds at a resolution of 120,000 (at m/z = 200). Fragmentation scans (MS2) were

497   acquired at 60,000 resolution between precursor scans by isolation of individual precursor ions

498   at 0.6 Th resolution, accumulation to 5 $\times 10^4$ automatic gain control for a maximum injection time

499   of 250 ms, and activation with beam collision (HCD) at 38% energy. Mass accuracy was

500   maintained throughout the experiment by internal calibrant lock mass.

501   The acquired data were searched against the SwissProt Human database by MASCOT

502   using 4 ppm and 0.01 Da precursor and fragment maximum mass error, respectively. TMT

503   labeled lysine and peptide N-termini and carbamidomethylation of cysteine were set as static

504   modifications. Oxidation of methionine and deamidation of asparagine and glutamine were set

505   as dynamic modifications. The results were rescored by Percolator in Proteome Discoverer 2.2

506   and quantitative analysis was carried out based on reporter ion intensities.

507   **Function Annotation**

508   We selected proteins with a protein abundance fold change (FC, *TAZ*$^{\Delta 45}$/ WT) less than or equal

509   to 0.80 (FC ≤ 0.80) and proteins with a FC greater than or equal to 1.2 (FC ≥ 1.20). Each subset

510   was individually uploaded to DAVID 6.8 and compared to the background "Homo sapiens" (18,

511   19). With the functional annotation tool, we pulled all KEGG pathways and GO terms for further

512   analysis.

513   **Quantitative RT-PCR**

514   Total RNA was extracted from an aliquot of 3 x 106 cells using the RNeasy Plus Kit (Qiagen).

515   cDNA was synthesized from extracted RNA using the iScript cDNA Synthesis Kit (BioRad) in 20

516   µl reactions according to the manufacturer's suggested protocol using 1 ug of RNA. cDNA was

517   subsequently diluted 10-fold with water. 2.4 µl of cDNA was analyzed in 12 µl reactions using

518   the SsoAdvanced Universal SYBR Green Supermix (Bio-Rad) according to the manufacturer's

519   instructions and included each respective forward and reverse gene-specific primers (Table

520   S12). Each sample-primer reaction was plated in triplicate per plate. Each plate also included

521   both no reverse-transcriptase controls (No-RT) for each cDNA sample and no template controls

522   (No-Template) for each primer pair. The reaction conditions were as follows: 2 min at 95°C,

16

523   followed by 40 two-temperature cycles of 5 s at 95°C and 30 s at 60°C. For nuclear genes,

524   expression of each gene was analyzed by the comparative CT (ΔΔCT) method with *TBP* and

525   *HPRT1* being averaged as endogenous reference genes. For mitochondrial genes (*MT-ND3)*,

526   expression of each gene was analyzed by the comparative CT (ΔΔCT) method with *MT-RNR1*,

527   *MT-CO1*, and *MT-ATP6* being averaged as endogenous reference genes. Values were

528   represented as average fold change relative to respective wildtype or untreated controls.

529   **1D BN-PAGE**

530   Cell pellets (100,000 cells, ~120ug) were solubilized for 30 min on ice in 20 mm Bis-Tris, 10%

531   glycerol, 50 mM NaCl, supplemented with 1% (v/v) Triton X-100 and protease inhibitors (PMSF,

532   Leupeptin, Pepstatin). Extracts were clarified by centrifugation for 30 min at 21 000g at 4C and

533   analyzed by 1D BN/SDS–PAGE as described by Claypool et al. (53).

534   **Complex I and II activity assays**

535   The activity of complex I was measured using the Complex I Enzyme Activity Microplate Assay

536   Kit (Abcam, #ab109721) according to the manufacturer's instructions using 200ug of isolated

537   mitochondria for both HEK293s and LCLs. The activity of complex II was measured using the

538   Complex II Enzyme Activity Microplate Assay Kit (Abcam, #ab109908) according to the

539   manufacturer's instructions using 200ug of isolated mitochondria for both HEK293s and LCLs.

540   **NDUFAF1 Transfection**

541   HEK293 cells were seeded into 15 cm plates. When cells reached ~80% confluency cells were

542   transiently transfected with *NDUFAF1*(NM_016013) C-Myc/DDK-tagged plasmid (Origene

543   #RC200029) with Lipofectamine 3000 (Thermo #L3000001) according to manufacturer's

544   instructions. 75.4 ug of plasmid was transfected with 105 uL of Lipofectamine 3000 per 15 cm

545   plate. The cells were grown in galactose media for 48hrs before mitochondria extraction

546   performed as described previously.

547   **Metabolomics**

548   HEK and LCL cell samples undergoing metabolic analysis were initially kept on ice and washed

549   with ice-cold PBS prior to collection, followed by centrifugation at 1500RPM and 4°C.

550   Metabolites within the cell pellet were extracted with 80% HPLC-grade methanol (Fisher

551   Scientific) and 20% mass-spec (MS)-grade water as previously described (54). The extraction

552   solution was then collected and evaporated using a speed-vac and a lyophilizer which resulted

553   in a white powder of dried metabolites. The collected metabolites were subsequently

554   resuspended in 50% (vol/vol) acetonitrile diluted with MS-grade water and analyzed via an

555   Agilent 1260 HPLC and 6490 triple-quadrupole (QQQ) mass spectrometer.

556   The Agilent 1260 HPLC-autosampler system was kept at 4°C for the entirety of the run

557   to prevent any degradation within the samples. Optimal separation was achieved with a reverse

558   phase chromatography system with an aqueous mobile phase of MS-grade water with 0.1%

559   formic acid and an organic mobile phase of 98% acetonitrile with 0.1% formic acid. The

560   Discovery® HS F5 HPLC Column (3µm particle size, L × I.D. 15 cm × 2.1 mm, Sigma) with a

561   compatible guard column (Sigma) were used and maintained at a temperature of 35°C. The

562   injection volume was 2µL and the runtime was 50 minutes per sample. The flow rate, buffer

563   gradient, and mass spectrometer parameters for the method were the same as previously

564   described (55).

565   Data from pure standards of each compound of interest were acquired prior and

566   simultaneously with samples in identical setting: precursor and product ion transitions, collision

567   energy, and ion polarity. Agilent MassHunter and Agilent Qualitative and Quantitative Analysis

568   Software packages were used to analyze the metabolic profiles. The metabolite peaks were

569   integrated for raw intensities and then normalized by protein concentration collected from the

570   original cell pellet. Protein concentration was determined using a FilterMax F5 microplate reader

571   and a Bovine Serum Albumin (BSA) standard.

572   **Data Analysis**

573   All statistical analyses were performed using R version 3.3.2 (2016-10-31) (56). Between-group

574   comparisons were performed using Welch's two-sample t-test. Outliers, outside 1.5x the

575   interquartile range above the upper quartile and below the lower quartile were only removed for

576   statistical analyses of the isogenic HEK293 cell lines.

577

18

587

588 **Conflict of Interest**

589 Hilary Vernon has received research support from Stealth BioTherapeutics.

590

591

592 **References**

593 1.   A. F. Anzmann, S. M. Claypool, H. Vernon, "Mitochondrial Dysfunction and Barth

594   Syndrome" in *Handbook of Mitochondrial Dysfunction*, S. I. Ahmad, Ed. (CRC

595   Press/Taylor & Francis Group, 2019), pp. 61–77.

596 2.   I. L. Gonzalez, Barth syndrome: TAZ gene mutations, mRNAs, and evolution. *Am. J.*

597   *Med. Genet.* **134 A**, 409–414 (2005).

598 3.   Y. W. Lu, *et al.*, Defining functional classes of Barth syndrome mutation in humans. *Hum.*

599   *Mol. Genet.* **25**, 1754–1770 (2016).

600 4.   Y. Xu, A. Malhotra, M. Ren, M. Schlame, The enzymatic function of tafazzin. *J. Biol.*

601   *Chem.* **281**, 39217–39224 (2006).

602 5.   P. Vreken, *et al.*, Defective remodeling of cardiolipin and phosphatidylglycerol in Barth

603   syndrome. *Biochem. Biophys. Res. Commun.* **279**, 378–382 (2000).

604 6.   W. Kulik, *et al.*, Bloodspot Assay Using HPLC – Tandem Mass Spectrometry for

605   Detection of Barth Syndrome. *Clin. Chem.* **54**, 371–378 (2008).

606 7.   P. G. Barth, *et al.*, An X-linked mitochondrial disease affecting cardiac muscle, skeletal

607   muscle and neutrophil leucocytes. *J. Neurol. Sci.* **62**, 327–355 (1983).

608 8.   C. Ferreira, R. Thompson, H. Vernon, "Barth Syndrome" in *GeneReviews®[Internet]*,

609   1993rd–2018th Ed., M. P. Adam, H. H. Ardinger, R. A. Pagon, S. E. Wallace, Eds.

610   (University of Washington, 2014) https:/doi.org/NBK247162 [bookaccession].

611 9.   A. E. Roberts, *et al.*, The Barth Syndrome Registry: Distinguishing disease characteristics

612   and growth data from a longitudinal study. *Am. J. Med. Genet. Part A* **158 A**, 2726–2732
613   (2012).

614   10.   W. R. Thompson, *et al.*, New targets for monitoring and therapy in Barth syndrome.
615   *Genet. Med.* **18**, 1001–1010 (2016).

616   11.   E. J. Lesnefsky, Q. Chen, C. L. Hoppel, Mitochondrial Metabolism in Aging Heart. *Circ.*
617   *Res.* **118**, 1593–1611 (2016).

618   12.   S. M. Claypool, C. M. Koehler, The complexity of cardiolipin in health and disease.
619   *Trends Biochem. Sci.* **37**, 32–41 (2012).

620   13.   L. K. Cole, *et al.*, Impaired cardiolipin biosynthesis prevents hepatic steatosis and diet-
621   induced obesity. *Diabetes* **65**, 3289–3300 (2016).

622   14.   Z. Younossi, *et al.*, Global burden of NAFLD and NASH: Trends, predictions, risk factors
623   and prevention. *Nat. Rev. Gastroenterol. Hepatol.* **15**, 11–20 (2018).

624   15.   K. Pfeiffer, *et al.*, Cardiolipin Stabilizes Respiratory Chain Supercomplexes. *J. Biol.*
625   *Chem.* **278**, 52873–52880 (2003).

626   16.   M. Zhang, E. Mileykovskaya, W. Dowhan, Gluing the respiratory chain together:
627   Cardiolipin is required for supercomplex formation in the inner mitochondrial membrane.
628   *J. Biol. Chem.* **277**, 43553–43556 (2002).

629   17.   M. McKenzie, M. Lazarou, D. R. Thorburn, M. T. Ryan, Mitochondrial Respiratory Chain
630   Supercomplexes Are Destabilized in Barth Syndrome Patients. *J. Mol. Biol.* **361**, 462–469
631   (2006).

632   18.   D. W. Huang, B. T. Sherman, R. A. Lempicki, Systematic and integrative analysis of large
633   gene lists using DAVID bioinformatics resources. *Nat. Protoc.* **4**, 44–57 (2009).

634   19.   D. W. Huang, B. T. Sherman, R. A. Lempicki, Bioinformatics enrichment tools: Paths
635   toward the comprehensive functional analysis of large gene lists. *Nucleic Acids Res.* **37**,
636   1–13 (2009).

637   20.   S. Guerrero-Castillo, *et al.*, The Assembly Pathway of Mitochondrial Respiratory Chain
638   Complex I. *Cell Metab.* **25**, 128–139 (2017).

639   21.   L. Stiburek, *et al.*, Knockdown of Human Oxa1l Impairs the Biogenesis of F1Fo-ATP
640   Synthase and NADH:Ubiquinone Oxidoreductase. *J. Mol. Biol.* **374**, 506–516 (2007).

641   22.   M. Spinazzi, B. De Strooper, PARL: The mitochondrial rhomboid protease. *Semin. Cell*
642   *Dev. Biol.* **60**, 19–28 (2016).

643   23.   G. Shi, G. A. McQuibban, The Mitochondrial Rhomboid Protease PARL Is Regulated by
644   PDK2 to Integrate Mitochondrial Quality Control and Metabolism. *Cell Rep.* **18**, 1458–
645   1472 (2017).

24. S. Saita, *et al.*, PARL mediates Smac proteolytic maturation in mitochondria to promote apoptosis. *Nat. Cell Biol.* **19**, 318–328 (2017).

25. C. Yang, *et al.*, Mitochondrial phosphatase PGAM5 regulates Keap1-mediated Bcl-xL degradation and controls cardiomyocyte apoptosis driven by myocardial ischemia/reperfusion injury. *Vitr. Cell. Dev. Biol. - Anim.* **53**, 248–257 (2017).

26. B. Wang, *et al.*, AMPKa2 protects against the development of heart failure by enhancing mitophagy via PINK1 phosphorylation. *Circ. Res.* **122**, 712–729 (2018).

27. S. Shires, Å. B. Gustafsson, Regulating Renewable Energy: Connecting AMPKα2 to PINK1/ Parkin-Mediated Mitophagy in the Heart. *Circ. Res.* **122**, 649–651 (2018).

28. C. Potting, *et al.*, TRIAP1/PRELI complexes prevent apoptosis by mediating intramitochondrial transport of phosphatidic acid. *Cell Metab.* **18**, 287–295 (2013).

29. X. Miliara, *et al.*, Structural determinants of lipid specificity within Ups/PRELI lipid transfer proteins. *Nat. Commun.* **10**, 1130 (2019).

30. L. Galluzzi, A. López-Soto, S. Kumar, G. Kroemer, Caspases Connect Cell-Death Signaling to Organismal Homeostasis. *Immunity* **44**, 221–231 (2016).

31. S. Sekine, *et al.*, Rhomboid protease PARL mediates the mitochondrial membrane potential loss-induced cleavage of PGAM5. *J. Biol. Chem.* **287**, 34635–34645 (2012).

32. Y. W. Lu, S. M. Claypool, Disorders of phospholipid metabolism: An emerging class of mitochondrial disease due to defects in nuclear genes. *Front. Genet.* **6** (2015).

33. A. Malhotra, *et al.*, Role of calcium-independent phospholipase A2 in the pathogenesis of Barth syndrome. *Proc. Natl. Acad. Sci.* **106**, 2337–2341 (2009).

34. H. H. Szeto, First-in-class cardiolipin-protective compound as a therapeutic agent to restore mitochondrial bioenergetics. *Br. J. Pharmacol.* **171**, 2029–50 (2014).

35. A. V. Birk, W. M. Chao, C. Bracken, J. D. Warren, H. H. Szeto, Targeting mitochondrial cardiolipin and the cytochrome c/cardiolipin complex to promote electron transport and optimize mitochondrial ATP synthesis. *Br. J. Pharmacol.* **171**, 2017–2028 (2014).

36. M. Zhang, E. Mileykovskaya, W. Dowhan, Cardiolipin is essential for organization of complexes III and IV into a supercomplex in intact yeast mitochondria. *J. Biol. Chem.* **280**, 29403–29408 (2005).

37. L. E. Formosa, M. G. Dibley, D. A. Stroud, M. T. Ryan, Building a complex complex: Assembly of mitochondrial respiratory chain complex I. *Semin. Cell Dev. Biol.* **76**, 154–162 (2018).

38. A. Picca, *et al.*, Mitochondrial quality control mechanisms as molecular targets in cardiac ageing. *Nat. Rev. Cardiol.* **15**, 543–554 (2018).

680 39. F. Fischer, A. Hamann, H. D. Osiewacz, Mitochondrial quality control: An integrated
681   network of pathways. *Trends Biochem. Sci.* **37**, 284–292 (2012).
682 40. H. B. Suliman, C. A. Piantadosi, Mitochondrial quality control as a therapeutic target.
683   *Pharmacol. Rev.* **68**, 20–48 (2016).
684 41. G. W. Dorn, Mitochondrial dynamism and heart disease: changing shape and shaping
685   change. *EMBO Mol. Med.* **7**, 865–77 (2015).
686 42. D. A. Stroud, *et al.*, Accessory subunits are integral for assembly and function of human
687   mitochondrial complex i. *Nature* **538**, 123–126 (2016).
688 43. A. Brown, *et al.*, Structures of the human mitochondrial ribosome in native states of
689   assembly. *Nat. Struct. Mol. Biol.* **24**, 866–869 (2017).
690 44. S. L. N. Clarke, *et al.*, Barth Syndrome. *Orphanet J. Rare Dis.* **8** (2013).
691 45. S. Lavandero, M. Chiong, B. A. Rothermel, J. A. Hill, Autophagy in cardiovascular
692   biology. *J. Clin. Invest.* **125**, 55–64 (2015).
693 46. E. Lee, *et al.*, Autophagy is essential for cardiac morphogenesis during vertebrate
694   development. *Autophagy* **10**, 572–87 (2014).
695 47. A. Saric, K. Andreau, A. S. Armand, I. M. Møller, P. X. Petit, Barth syndrome: From
696   mitochondrial dysfunctions associated with aberrant production of reactive oxygen
697   species to pluripotent stem cell studies. *Front. Genet.* **6**, 359 (2016).
698 48. D. V. Jeyaraju, H. M. McBride, R. B. Hill, L. Pellegrini, Structural and mechanistic basis of
699   Parl activity and regulation. *Cell Death Differ.* **18**, 1531–1539 (2011).
700 49. L. Ozgyin, A. Horvath, Z. Hevessy, B. L. Balint, Extensive epigenetic and transcriptomic
701   variability between genetically identical human B-lymphoblastoid cells with implications in
702   pharmacogenomics research. *Sci. Rep.* **9**, 4889 (2019).
703 50. F. A. Ran, *et al.*, Genome engineering using the CRISPR-Cas9 system. *Nat. Protoc.*
704   (2013) https:/doi.org/10.1038/nprot.2013.143.
705 51. P. D. Hsu, *et al.*, DNA targeting specificity of RNA-guided Cas9 nucleases. *Nat.*
706   *Biotechnol.* **31**, 827–832 (2013).
707 52. F. M. Vaz, *et al.*, Mutations in PCYT2 disrupt etherlipid biosynthesis and cause a complex
708   hereditary spastic paraplegia. *Brain* **142**, 3382–3397 (2019).
709 53. S. M. Claypool, Y. Oktay, P. Boontheung, J. A. Loo, C. M. Koehler, Cardiolipin defines
710   the interactome of the major ADP/ATP carrier protein of the mitochondrial inner
711   membrane. *J. Cell Biol.* **182**, 937–950 (2008).
712 54. A. Elgogary, *et al.*, Combination therapy with BPTES nanoparticles and metformin targets
713   the metabolic heterogeneity of pancreatic cancer. *Proc. Natl. Acad. Sci. U. S. A.* **113**,

714   E5328–E5336 (2016).

715 55.   T. Nguyen, *et al.*, Uncovering the Role of N-Acetyl-Aspartyl-Glutamate as a Glutamate

716   Reservoir in Cancer. *Cell Rep.* **27**, 491–501 (2019).

717 56.   R Core Team, R: A language and environment for statistical computing.No Title (2016).

718
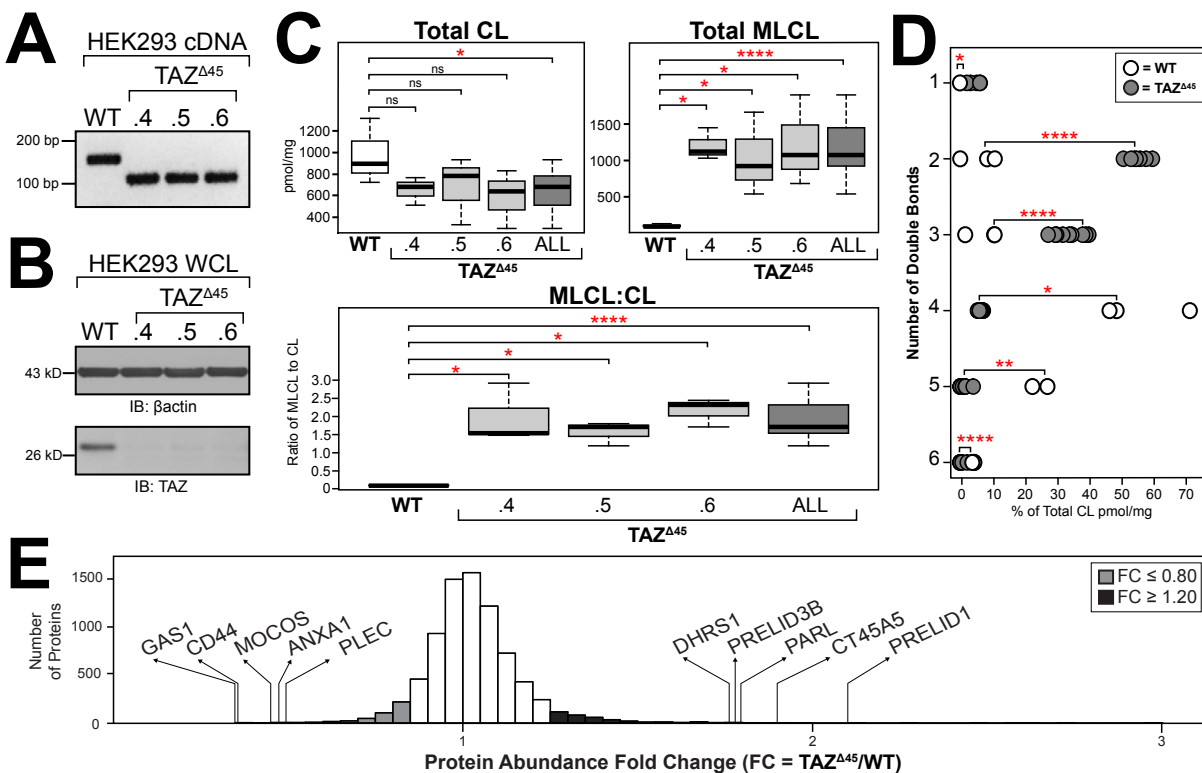
Figure 1. $TAZ^{\Delta 45}$ HEK293 genetic characterization, CL profiling and proteomics analysis.
(A) RT-PCR of RNA extracted from the HEK293 $TAZ^{\Delta 45}$ clones using primers specific to the region of *TAZ* being edited. **(B)** Whole cells lysate (45ug) of the indicated lines immunoblotted for TAZ and loading control β-actin. **(C)** The abundance of CL and MLCL in WT (n=3) and $TAZ^{\Delta 45}$ clones (n=3, per clone) was determined by shotgun lipidomics via mass spectrometry. **(D)** The distribution of double bonds across CL species was determined as a percentage of total CL. **(E)** 7713 proteins were identified and quantified with TMT 10-plex mass spectrometry of whole cell lysate (200ug) of $TAZ^{\Delta 45}$ (n=3) and WT cells (n=3). Protein abundance fold change (FC) calculated by dividing the average abundance per protein identified in $TAZ^{\Delta 45}$ cells by WT average abundance per protein. The genes that encode the most significantly reduced proteins in $TAZ^{\Delta 45}$ cells are *GAS1* (FC=0.35, p=2.5 x 10-4), *CD44* (FC=0.367, p=6.6 x 10-4), *MOCOS* (FC=0.45, p=0.011), *ANAX1* (FC=0.478, p=0.01) , and *PLEC* (FC=0.491, p=2.7 x 10-4). The genes that encode the most significantly increased proteins in $TAZ^{\Delta 45}$ cells are *PRELID1* (FC=2.125, p=8.4 x 10-4), *CT45A5* (FC=1.909, p=0.023), *PARL* (FC=1.815, p=0.016), *PRELID3B* (FC=1.795, p=3.9 x 10-4), and *DHRS1* (FC=1.774, p=0.016). Proteins with a fold change (FC) ≤ 0.80 are highlighted in grey (n=215) and proteins with a FC ≥ 1.20 are highlighted in black (n=621). Significant differences are indicated; * ≤ 0.05, ** ≤ 0.005, *** ≤ 0.0005, **** ≤ 0.00005.

24
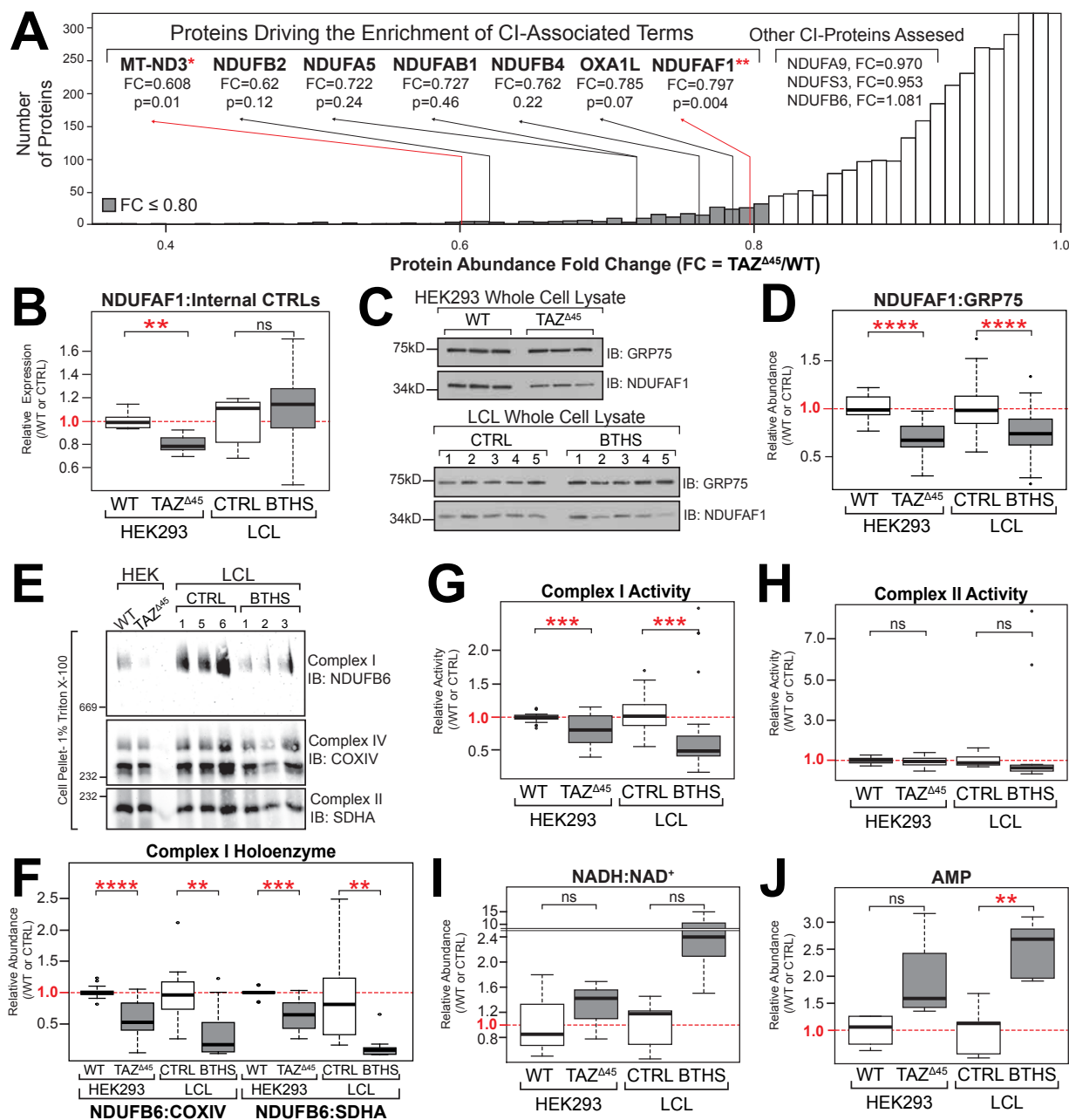
Figure 2. Reduced complex I (CI) holoenzyme abundance and activity in HEK293 _TAZ_$^{\Delta45}$ cells and BTHS patient-derived lymphoblastoid cells. (A) The enrichment of the CI-associated terms is driven by 7 genes; _MT-ND3_, _NDUFAF1_, _NDUFA5_, _NDUFAB1_, _NDUFB2_, _NDUFB4_, _OXA1L_. **(B)** Relative mRNA expression of _NUDFAF1_, determined by qRT-PCR and $\Delta\Delta C_T$ quantification. Data plotted relative to WT/CTRL expression; WT n=6, _TAZ_$^{\Delta45}$ n=6, CTRL n=10, BTHS n=15. **(C)** Whole cell lysate (45 ug) of the indicated lines were immunoblotted for the indicated proteins. **(D)** Band intensities, relative to the loading control GRP75, were quantified and plotted relative to WT/CTRL abundance; WT n=27, _TAZ_$^{\Delta45}$ n=26, CTRL n=49, BTHS n=48.

25

746 **(E)** BN-PAGE of HEK293 WT and $TAZ^{\Delta 45}$ or CTRL and BTHS LCL cells (100-250K cells)

747 solubilized in 1% Triton X-100 immunoblotted for the indicated proteins. **(F)** Band intensities were

748 quantified, and CI abundance was represented as the ratio of CI band intensity to CIV (COXIV)

749 or CII (SDHA). Abundance was plotted relative to WT/CTRL abundance; CI:CIV(WT n=13, $TAZ^{\Delta 45}$

750 n=16, CTRL n=12, BTHS n=12), CI:CII (WT n=10, $TAZ^{\Delta 45}$ n=13, CTRL n=9, BTHS n=9). **(G)** CI

751 activity measured in HEK293 WT and $TAZ^{\Delta 45}$ or CTRL and BTHS LCLs mitochondria (200 ug total

752 protein) on a microplate reader (450nm) by following the oxidation of NADH to oxidized

753 nicotinamide adenine dinucleotide (NAD+). Activity plotted relative to WT/CTRL abundance; WT

754 n=25, $TAZ^{\Delta 45}$ n=26, CTRL n=36, BTHS n=42. **(H)** CII activity measured in HEK293 WT and $TAZ^{\Delta 45}$

755 or CTRL and BTHS LCLs mitochondria (200 ug total protein) on a microplate reader by following

756 the production of ubiquinol by CII coupled to the reduction of the dye diclorophenolindophenol

757 (DCPIP, 600nm). Activity plotted relative to WT/CTRL abundance; WT n=12, $TAZ^{\Delta 45}$ n=12, CTRL

758 n=10, BTHS n=12. Targeted metabolomics was used to measured **(I)** NADH, NAD+, and **(J)**

759 cellular AMP via mass spectrometry in HEK293 WT (n=3), HEK293 $TAZ^{\Delta 45}$ (n=3), CTRL LCL

760 (n=5) and BTHS LCL (n=5) cells. Significant differences are indicated; * ≤ 0.05, ** ≤ 0.005, *** ≤

761 0.0005, **** ≤ 0.00005.
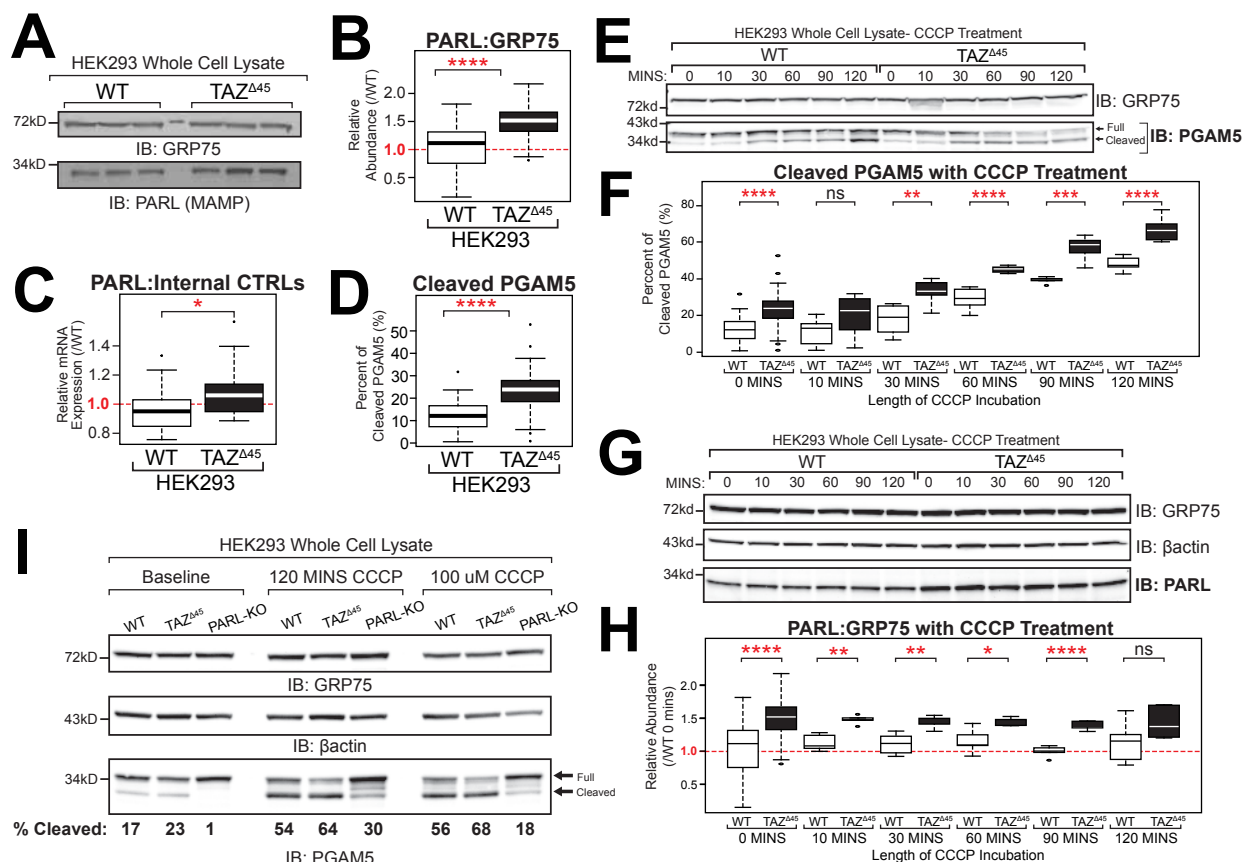
Figure 3. Increased cleavage of PGAM5 by PARL in HEK293 $TAZ^{\Delta45}$ cells. (A) Whole cell lysate (45 ug) of the indicated lines were immunoblotted for the indicated proteins. **(B)** Band intensities, relative to loading control GRP75, were quantified and plotted relative to WT abundance; WT n=54, $TAZ^{\Delta45}$ n=48 **(C)** Relative mRNA expression of *PARL* determined by qRT-PCR and $\Delta\Delta C_T$ quantification; WT n=18, $TAZ^{\Delta45}$ n=17. **(D)** Whole cell lysate (45 ug) of WT and $TAZ^{\Delta45}$ cells were immunoblotted for PGAM5 and loading control GRP75. Band intensities, relative to the loading control GRP75, for both full-length and cleaved PGAM5 were individually quantified and plotted as the percent of cleaved PGAM5 (cleaved/full+cleaved); WT n=41, $TAZ^{\Delta45}$ n=41. **(E)** HEK293 WT and $TAZ^{\Delta45}$ cells were treated with 20uM CCCP for serial time points from 0 to 120 minutes. Whole cell lysate (45 ug) of the indicated lines and treatment times were immunoblotted for the indicated proteins. **(F)** Band intensities, relative to the loading control GRP75, for both full-length and cleaved PGAM5 were individually quantified and plotted as the percent of cleaved PGAM5 (cleaved/full+cleaved); WT 0 mins n=41, WT 10 mins n=8, WT 30 mins n=8, WT 60 mins n=8, WT 90 mins n=5, WT 120 mins n=7, $TAZ^{\Delta45}$ 0 mins n=41, $TAZ^{\Delta45}$ 10 mins n=8, $TAZ^{\Delta45}$ 30 mins n=7, $TAZ^{\Delta45}$ 60 mins n=5, $TAZ^{\Delta45}$ 90 mins n=7, $TAZ^{\Delta45}$ 120 mins n=7. **(G)** HEK293 WT and $TAZ^{\Delta45}$ cells were treated with 20uM CCCP for serial time points from 0 to

27

779   120 minutes. Whole cell lysate (45 ug) of the indicated lines and treatment times were

780   immunoblotted for the indicated proteins. **(H)** Band intensities, relative to the loading control

781   GRP75, were quantified and plotted relative to WT abundance; WT 0 mins n=54, WT 10 mins

782   n=5, WT 30 mins n=6, WT 60 mins n=6, WT 90 mins n=5, WT 120 mins n=6, $TAZ^{\Delta45}$ 0 mins n=48,

783    $TAZ^{\Delta45}$ 10 mins n=5, $TAZ^{\Delta45}$ 30 mins n=5, $TAZ^{\Delta45}$ 60 mins n=5, $TAZ^{\Delta45}$ 90 mins n=5, $TAZ^{\Delta45}$ 120

784   mins n=6. **(I)** Whole cell lysate (45 ug) of the indicated lines were immunoblotted for the indicated

785   proteins. Band intensities, relative to the loading control GRP75, for both full-length and cleaved

786   PGAM5 were individually quantified, and the percent of cleaved PGAM5 (cleaved/full+cleaved) is

787   indicated for each lane (n=1). Significant differences are indicated; * ≤ 0.05, ** ≤ 0.005, *** ≤

788   0.0005, **** ≤ 0.00005.

789
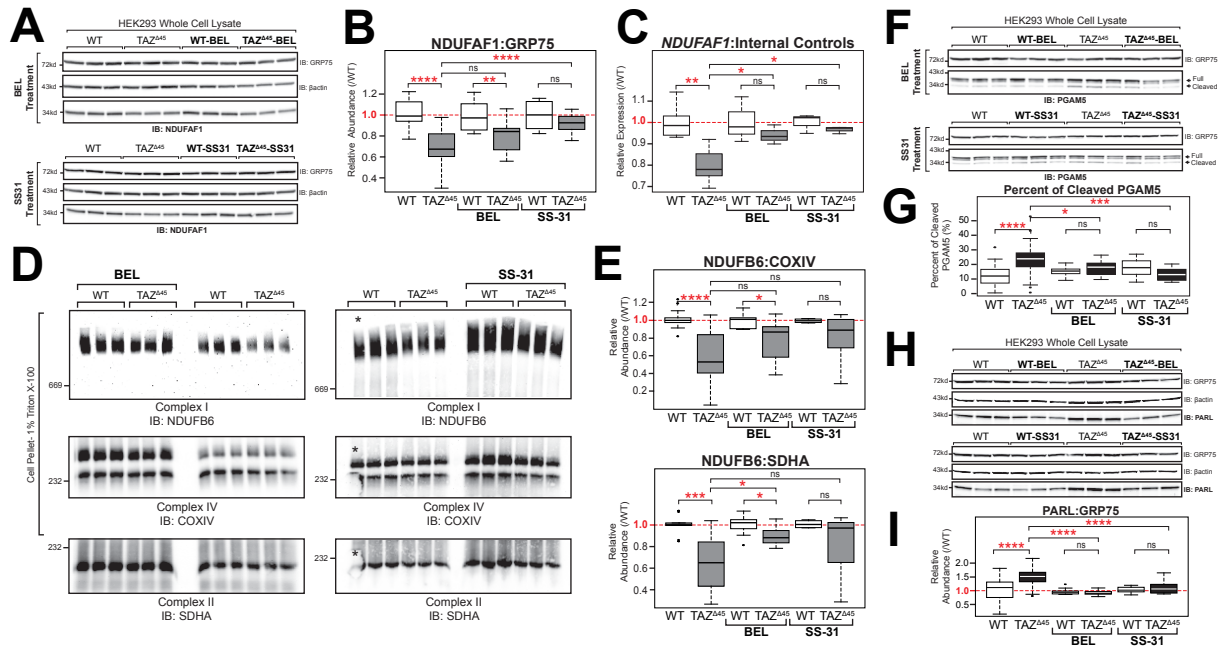
Figure 4. Targeting CL or CL metabolism with bromoenol lactone and SS-31 modifies mitochondrial dysfunction. (A) HEK293 WT and $TAZ^{\Delta45}$ cells were treated for 48 hours with 2.5uM bromoenol lactone (BEL) and 7 days with 100nM SS-31. Whole cell lysate (40-45 ug) of the indicated lines were immunoblotted for the indicated proteins. **(B)** Band intensities, relative to the loading control GRP75, were quantified and plotted relative to WT abundance; WT n=27, $TAZ^{\Delta45}$ n=26, WT-BEL n=9, $TAZ^{\Delta45}$-BEL n=9, WT-SS-31 n=9, $TAZ^{\Delta45}$-SS-31 n=9. **(C)** Relative mRNA expression of *NDUFAF1* determined by qRT-PCR and $\Delta\Delta C_T$ quantification using each respective control; WT n=6, $TAZ^{\Delta45}$ n=3, WT-BEL n=3, $TAZ^{\Delta45}$-BEL n=3, WT-SS-31 n=3, $TAZ^{\Delta45}$-SS-31 n=3 per gene. **(D)** BN-PAGE of HEK293 WT and $TAZ^{\Delta45}$ cells treated for 48 hrs with 2.5uM BEL (120 ug total protein) and 7 days with 100nM SS-31 solubilized in 1% Triton X-100 immunoblotted for the indicated proteins. All samples were resolved on a single gel and exposed for the same duration. The WT lane indicated with the asterisk was not used for quantification due to air bubbles. **(E)** Band intensities were quantified, and CI abundance was represented as the ratio of CI band intensity to CIV or CII. Abundance was plotted relative to respective control; CI:CIV(WT n=13, $TAZ^{\Delta45}$ n=16, WT-BEL n=9, $TAZ^{\Delta45}$-BEL n=11, WT-SS-31 n=4, $TAZ^{\Delta45}$-SS-31 n=6), CI:CII (WT n=10, $TAZ^{\Delta45}$ n=13, WT-BEL n=9, $TAZ^{\Delta45}$-BEL n=10, WT-SS-31 n=4, $TAZ^{\Delta45}$-SS-31 n=6). **(F)** Whole cell lysate (40-45 ug) of the indicated lines and treatment conditions were immunoblotted for the indicated proteins. **(G)** Band intensities, relative to the loading control GRP75, for both full-length and cleaved PGAM5 were individually quantified and plotted as the percent of cleaved PGAM5 (cleaved/full+cleaved); WT n=41, $TAZ^{\Delta45}$ n=41, WT-BEL n=16,

811 *TAZ*$^{\Delta45}$-BEL n=16, WT-SS-31 n=9, *TAZ*$^{\Delta45}$-SS-31 n=8. **(H)** Whole cell lysate (40-45 ug) of the

812 indicated lines and treatment conditions were immunoblotted for the indicated proteins. **(I)** Band

813 intensities, relative to the loading control GRP75, were quantified and plotted relative to WT

814 abundance; WT n=54, *TAZ*$^{\Delta45}$ n=48, WT-BEL n=11, *TAZ*$^{\Delta45}$-BEL n=11, WT-SS-31 n=10, *TAZ*$^{\Delta45}$-

815 SS-31 n=12. Significant differences are indicated; * ≤ 0.05, ** ≤ 0.005, *** ≤ 0.0005, **** ≤ 0.00005.

816